A Dual-Scale Model for Describing Drier and Porous Medium Interactions

Patrick Perré
Laboratory of Wood Science (LERMAB), UMR 1093 INRA/French Institute of Forestry, Agricultural and Environmental Engineering (ENGREF), Université Henri Poincaré, ENGREF, F-54042 Nancy Cedex, France

Ian W. Turner
School of Mathematical Sciences, Queensland University of Technology, Brisbane, Q4001, Australia

DOI 10.1002/aic.10918
Published online July 5, 2006 in Wiley InterScience (www.interscience.wiley.com).

A dual-scale modeling approach is proposed to describe the coupling of the drier (large-scale) and the porous medium (macroscale) throughout drying. This model is used to investigate the vacuum drying of a softwood board placed in an experimental vacuum chamber that is heated by two infrared (IR) emitters. The large-scale model provides important information for the drying engineer to assess and tune the performance of the drier. This model allows simulation of the chamber wall and IR emitter temperature evolution, together with changes in the chamber vapor, air, and water mass balances. The comprehensive two-dimensional drying model known as TransPore is used to determine the heat and mass transfer occurring at the macroscale of the board. Finally, four case studies are presented to elucidate the intricate coupling that exists between the chamber technical specifications and the drying behavior of the porous medium. A highlight of the dual-scale model is its ability to predict the condensation on the walls of a poorly insulated vacuum chamber for the case of a weak pump. © 2006 American Institute of Chemical Engineers *AIChE J,* 52: 3109–3117, 2006
Keywords: two-dimensional heat and mass transfer, vacuum chamber model, experimental data, kiln-load coupling

Introduction

It is now well accepted that vacuum drying of wood offers reduced drying times and higher end-product quality compared with that of conventional drying operations.[1] The reduction in the boiling point of water at low pressure facilitates an important overpressure generated within the product to enhance moisture migration. High-quality hardwoods such as oak[2,3] and Australian eucalyptus[4,5]—that are difficult to dry conventionally—are often dried under vacuum to avoid collapse and discoloration.

The complexities of reducing the external pressure during drying on the transfer phenomena evolving within wood have been the focus of a number of previous studies.[6-9] Most important, however, it is the lowering of the external energy transfer under vacuum and the identification of an effective mechanism for heating the product that constitute an open question that still remains to be answered. Conventional vacuum dryers overcome this problem either using a discontinuous process of alternating phases of vacuum drying with phases of convective heating under atmospheric pressure or drying under vacuum with heated plates positioned between boards.[10] Some other possibilities are high vacuum drying[2] and radio-frequency heating, which is known to be optimal in terms of process control and ensures that the pressure level and heat supplied to the load are delivered independently.[11,12] The ap-

Correspondence concerning this article should be addressed to P. Perré at perre@engref.fr.

plication given here concerns vacuum drying with radiative heating, which is a process commonly used in the paper industry but seldom used for wood drying because of the geometry of the stacks, which are not readily adapted to this type of heating. It is thought that radiative devices arranged between layers of boards could offer better performance than that of heated plates if they are designed in such a way that the path for the moisture remains free at the surface of the boards.

This work sets forth the development of a coupled dual-scale computational model that can be used to predict the vacuum drying of wood placed in a small prototype industrial dryer.[13] It builds on, in a natural way, the foundation modeling work for vacuum drying previously published by Turner and Perré[14], by providing a much more realistic description of the vacuum chamber and wood interactions throughout the vacuum drying process. The computational model embeds an existing porous medium model within the large-scale drying model,[15] enabling the evolution of the masses of vapor, air, and water in the chamber, together with the temperatures of the vacuum chamber and the IR emitters, to be predicted throughout the drying process. Such a model enables condensation on the kiln walls to be accounted for in the evolution of the relative humidity within the chamber. The inclusion of this phenomenon within the kiln-scale model enables a wide range of drying processes to be simulated and, most important, paves the way for online kiln control. Knowledge of the vacuum chamber vapor pressure at any given instant throughout the simulation is imperative for studying the coupling that exists between the product and the drier. The link between the two scales is achieved by the boundary conditions that are imposed at the surface of the porous medium (large-scale to macroscale interaction) and by the total heat, vapor, and air fluxes leaving the board (macroscale to large-scale interaction).

This article is organized as follows. In the next section we give details of the experimental configuration, after which the mathematical formulation and underlying computational strategies are outlined. Thereafter, the simulation results for four case studies concerning the vacuum drying of fir sapwood are presented, along with the experimental measurements used to assess the accuracy of the model. Finally, the conclusions of the work are summarized and we hint at future research directions.

Experimental

The vacuum drying experiments were performed at the Laboratory of Forest Sciences (LERMAB), ENGREF in Nancy, France. A softwood board was placed into a pressure tank between two IR emitters with reflectors, as shown in Figure 1. Far IR radiation with a temperature close to 600 K was obtained by supplying classical quartz tubes with low voltage. A membrane vacuum pump was used to remove full water vapor from the chamber during the experiment. The pump allowed the condensation of water at the outlet of the pump to be collected and weighed to determine the moisture removed from the board during drying. This configuration made it possible to recover on balance up to 95% of the weight loss of the board.[13]

Another key innovation of the experimental configuration was the simultaneous measurement of both temperature and pressure at the same location. Measurements were made using a new version of the sensor, developed originally for convective drying at high temperature.[16] Pressure and temperature are still measured at the same location, but the addition of a thread and two O-rings sealed against the epoxy resin ensures a better airtightness throughout the process. These new sensors are larger (4 mm in diameter instead of 1.1 mm) than the original design and induce more perturbations. In particular, it is no longer possible to position several sensors along the board thickness in the same section. Here, two locations were studied, both near the half-length of the board: one at the center (half-thickness) and the other, called "surface," as close as possible to the exchange surface (≈4–5 mm). The connections of the pressure gauge are such that the difference of pressure between the board and the surrounding gas is measured. To reduce the air volume and, above all, to avoid condensation in the pressure gauges, the tubes are filled with oil from very close to the board up to the pressure gauge, which is situated outside the vacuum chamber (refer to Perré et al.[13] for full details).

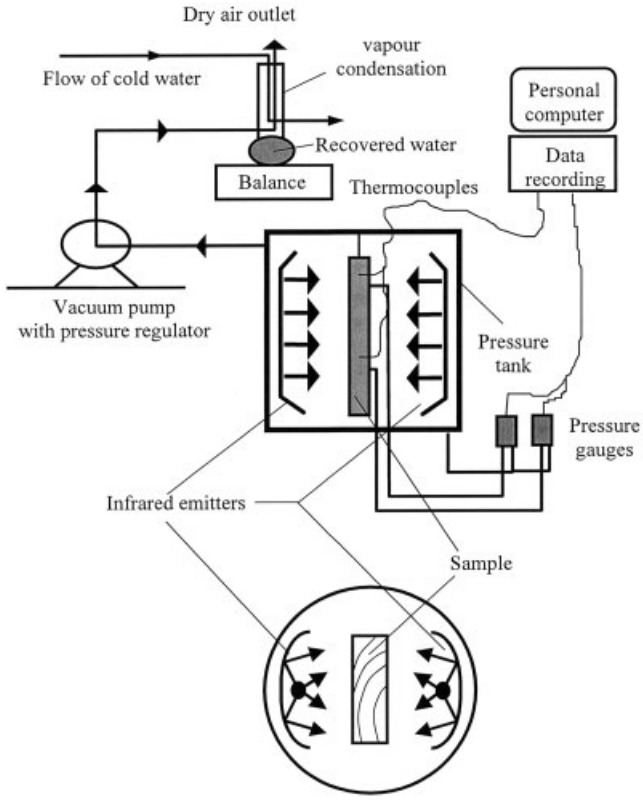

Figure 1. Vacuum drying configuration.

Mathematical Formulation

The key aspects of the dual-scale modeling approach were reported recently at the 14th International Drying Symposium held in Brazil and documented briefly in the conference proceedings.[14] For completeness, we provide full details of the large-scale drier model again in this section and provide only a summary of the macroscopic heat and mass transfer model in Appendix A. The interested reader can find more comprehensive details of the wood drying model in previous research work conducted by the authors.[17-20,22,23] The physical parameters used in the macroscopic transport equations are strongly dependent on the wood species. The properties used for all

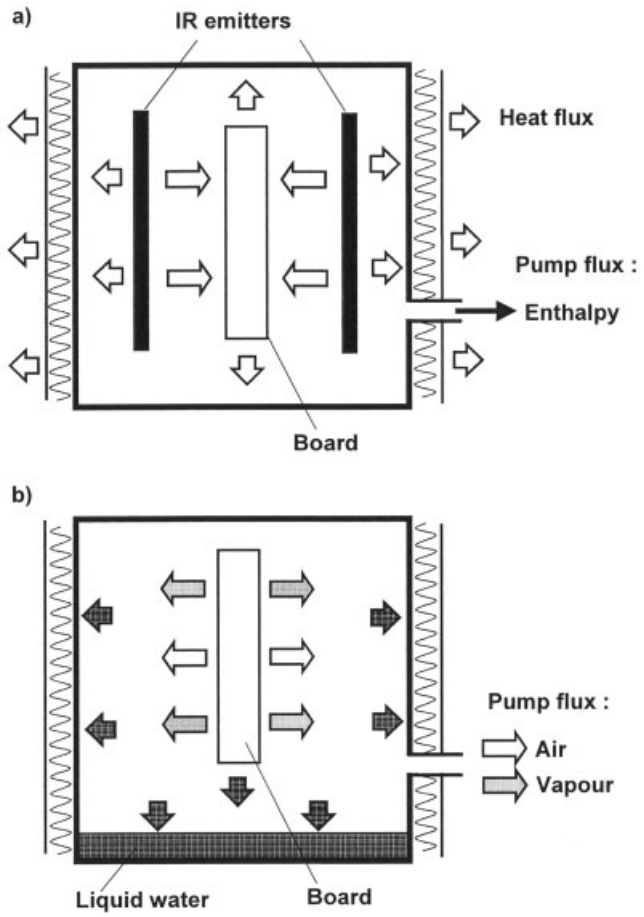

Figure 2. Chamber model.

(a) Enthalpy balance; (b) mass balance.

simulations reported here were taken directly from the literature (see, for example, Perré and Turner[20,23]) and are summarized in Appendix B. The permeability values used for softwood in transverse and longitudinal directions were taken from a previous article on vacuum drying.[24]

Vacuum chamber model

The air, vapor, and water mass balance equations are derived by assuming that the pressure and temperature fields within the chamber are homogeneous. Using a control volume that includes the surfaces of the wood sample, together with the walls of the vacuum chamber and the IR emitters, the following balance equations for the vacuum chamber (Figures 2a and 2b) are obtained:

Air Mass Balance

$$\frac{dm_a}{dt} = -\rho_a^{(ch)} Q_{pump} + F_a^{(wood)} A^{(ws)} \tag{1}$$

Vapor Mass Balance

$$\frac{dm_v}{dt} = -\rho_v^{(ch)} Q_{pump} + F_v^{(wood)} A^{(ws)} + F_w^{(ch)} A^{(ev)} \tag{2}$$

Water Mass Balance

$$\frac{dm_w}{dt} = F_w^{(wood)} A^{(ws)} + \begin{cases} F_w^{(ch)} A^{(ch)} & \text{if condensation state} \\ -F_w^{(ch)} A^{(ev)} & \text{if evaporation state} \end{cases} \tag{3}$$

In the mass balance Eqs. 1–3 the variables m_a, m_v, and m_w represent, respectively, the masses of air, vapor, and water in the chamber and $\rho_a^{(ch)}$ and $\rho_v^{(ch)}$ represent the densities of air and vapor in the chamber. Q_{pump} is the flow rate of the pump; $F_a^{(wood)}$, $F_v^{(wood)}$, and $F_w^{(wood)}$ are the total fluxes of air, vapor, and liquid leaving the board; and $A^{(ws)}$ is the total surface area of the board. $F_w^{(ch)}$ represents the flux of water in the chamber arising from condensation or evaporation; and $A^{(ch)}$ and $A^{(ev)}$ are, respectively, the surface area of the vacuum chamber and the total surface area within the chamber open for evaporation, which in this case is the circular bottom of the vacuum chamber.

The energy balance equations for the chamber and the IR emitters are as follows:

Chamber Energy Balance

$$\frac{d}{dt}(m_a e_a + m_v e_v + m_w e_w + m_{ch} e_{ch}) = -[\rho_a^{(ch)} h_a + \rho_v^{(ch)} h_v] Q_{pump} + F_H A^{(ws)} + [F_{ch\to IR}\sigma(T_{IR}^4 - T_{ch}^4) + F_{ch\to w}\sigma(T_{w_{eq}}^4 - T_{ch}^4) + h(T_{ext} - T_{ch})] A^{(ch)} \tag{4}$$

Emitter Energy Balance

$$\frac{d}{dt}(m_{IR} e_{IR}) = [F_{IR\to ch}\sigma(T_{ch}^4 - T_{IR}^4) + F_{IR\to w}\sigma(T_{w_{eq}}^4 - T_{IR}^4)] A^{(IR)} + E_{pwr} \tag{5}$$

Here, m_{ch} and m_{IR} represent the masses of the chamber walls and the IR emitters and $A^{(IR)}$ represents the surface area of the IR emitter. T_{ch} and T_{IR} are the temperatures of the chamber and the IR emitters and e_a, e_v, e_w, e_{ch}, and e_{IR} are the internal specific energies of the air, vapor, water, chamber, and IR emitters. h_a and h_v are the specific enthalpies of the air and vapor in the chamber and F_H is the total convective heat flux from the board to the chamber. E_{pwr} represents the input electrical power of the system, σ is the Stefan–Boltzmann constant, and h is the external convective heat transfer coefficient. The view factors $F_{ch\to IR}$, $F_{ch\to w}$, $F_{IR\to ch}$, and $F_{IR\to w}$ were estimated from Bird et al.[6] for the case of two parallel plates. The internal energies of the air and vapor phases can be written as $e = h - P\nu$, where ν is the specific volume and P is pressure. Note that the internal energies and the enthalpies of all other variables are equal.

Pressure in the chamber is computed according to the ideal gas law. The enthalpies of each phase are determined by assuming that the gas and liquid phases in the chamber equal the chamber wall temperature. Enthalpies of the chamber walls and the IR emitters are assumed to equal the product of the specific heat of stainless steel and its temperature. The flux of water in the chamber is controlled using a set of rules that enables a condensation state $[P_v^{(ch)} > P_{vs}^{(ch)}]$ or an evaporation state to exist.

Interfacial Boundary Conditions. The total liquid flux ($\mathbf{J_w}$) and energy flux ($\mathbf{J_e}$) boundary conditions imposed at the external drying surfaces of the wood sample are, respectively

$$\mathbf{J_w} \cdot \hat{\mathbf{n}} = k_m c M_v \ln\left[\frac{1 - x_v^{(ch)}}{1 - x_v}\right]$$

$$\mathbf{J_e} \cdot \hat{\mathbf{n}} = F_{w\to ch}\sigma(T^4 - T_{ch}^4) + F_{w\to IR}\sigma(T^4 - T_{IR}^4) + h_v k_m c M_v \ln\left[\frac{1 - x_v^{(ch)}}{1 - x_v}\right] \quad (6)$$

where x_v and T are, respectively, the molar fraction of the gas vapor and the temperature at the exchange surfaces. The corresponding variables labeled (*ch*) indicate quantities that are characteristic of the vacuum chamber. Equation 11 reveals one sense of the coupling, from the chamber to the load. The quantity k_m is an appropriately defined mass transfer coefficient and the view factors $F_{w\to ch}$ and $F_{w\to IR}$ have again been estimated. Noted that in the case of pure vapor within the chamber, this form of boundary conditions imposes an equality of the wood surface vapor pressure and the vacuum chamber vapor pressure as a result of the singularity that arises in the log function. The pressure at the external drying surfaces is fixed at the vacuum chamber pressure. Symmetry planes are introduced to reduce the overall computation times. For the wood sample under consideration here, the computational domain represents only one quarter. Initially, the porous medium has some prescribed moisture and temperature distributions, with the pressure being constant throughout at the atmospheric value. The vapor pressure of the chamber and the temperatures of the chamber and the IR emitters are assumed initially to be at ambient conditions.

Numerical Solution Procedure

Macroscale porous medium model

The numerical procedure used for stepping the macroscale drying equations in time has been documented extensively over the last decade and the interested reader is referred to previous studies[19,22,23] for more comprehensive details. Briefly, the numerical strategy uses the finite-volume method to discretize the conservation laws and an efficient Inexact Newton method is used to solve the resulting large and sparse discrete nonlinear system that describes the drying process. Flux limiting is used for the spatial weighting scheme for all advection/convection terms to reduce numerical dispersion of the drying fronts.

Large-scale drier model

The kiln-scale system of differential Eqs. 1–5 is integrated in time using an implicit first-order scheme, which results in a discrete nonlinear system expressed in the form $\mathbf{F}(\mathbf{u}) = [F_a(\mathbf{u}), F_v(\mathbf{u}), F_w(\mathbf{u}), F_{ch}(\mathbf{u}), F_{IR}(\mathbf{u})]^T = \mathbf{0}$, where $\mathbf{u} = [\rho_a^{(ch)}, \rho_v^{(ch)}, m_w, T_{ch}, T_{IR}]^T$. The coordinate functions are complicated nonlinear functions of the chamber variables and its state. This nonlinear system must be solved, at each time step, to advance all of the chamber variables in time.

The solution procedure is carried out in two distinct stages by *outer* and *inner* iteration. During the outer iteration phase, the system of nonlinear equations is linearized according to an Inexact Newton scheme. The estimate of the solution vector at the $(n + 1)$th level is computed from the current solution at the nth level by writing $\mathbf{u}^{(n+1)} = \mathbf{u}^{(n)} + \lambda^{(n)} d\mathbf{u}^{(n)}$ and solving the system of linearized equations $\mathbf{J}[\mathbf{u}^{(n)}]d\mathbf{u}^{(n)} = -\mathbf{F}[\mathbf{u}^{(n)}]$ for the Newton correction vector $\delta\mathbf{u}^{(n)}$. Here $\mathbf{J}$ represents an approximation to the true Jacobian matrix and the derivatives needed for its construction are computed numerically using finite-difference approximations (similar to that discussed in Turner and Perré[19]). For the system under investigation here, the Jacobian matrix is dense and of dimension 5×5. This system is solved using an efficient *LU* decomposition method that uses implicit scaled partial pivoting. The length of the Newton step $\lambda^{(n)}$ is determined using line searching.[25]

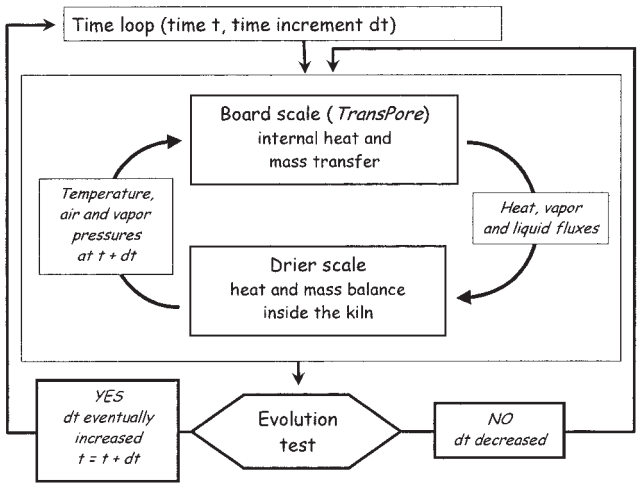

Figure 3. Coupling between the two scales: the convergence strategy.

Coupling between the two scales

During the simulation each of the dual-scale models has its own solver and adaptive time stepping procedure. The link between the two scales evolves according to the chamber conditions through the boundary conditions imposed at the surface of the porous medium (large-scale → macroscale) and by the total heat, vapor, air, and, eventually, liquid fluxes leaving the board (large-scale ← macroscale).

The adaptive time-stepping strategy used for each solver is critical to the convergence of the dual-scale model. Both must be regulated in a manner that ensures that the gas dynamics evolving in the chamber and the coupled heat, mass, and momentum transfers occurring within the board do not dramatically change during the time increment selected by the dual-scale model (see Figure 3). The chamber dynamics is primarily driven by the fluxes leaving the board, the pump flow rate when switched on, and the eventual rate of condensation on the chamber walls. In practice and for the experimental chamber under consideration herein, the chamber dynamics usually has a time constant much smaller than the internal transfer arising within the board. This is especially the case when a strong pump is switched on. In such conditions, the dynamics and the convergence conditions of the board result mainly from the rapid change of the boundary conditions. One can imagine the

dramatic effect of the change of the external pressure on internal transfer when, for instance, a liquid flow is driven by the internal overpressure (high-temperature configuration). The board macroscale model must be able to capture such a coupling and, in turn, supply the chamber model with relevant values of the different fluxes leaving the board. As a result of this coupling between the two scales, the time step of the dual-scale model is much smaller than that used for the macroscale model. Although the number of degrees of freedom is considerably low in the large-scale model compared to that in the macroscale model (*TransPore*), the CPU time of the dual-scale model with a strong pump is typically 6 min when running on a 2.8-GHz Xeon processor. For the sake of comparison, the 2-D version of *TransPore* alone needs only around 20 s on the same machine. Great care was also paid to the way in which the results were saved to a data file. The rapid variation of the chamber conditions, such as the pressure, could be captured only by the use of a dramatically high sampling frequency, which results in extremely large data files. Instead, a double-writing instruction was used, whereby the results are saved at a reasonable frequency, as well as each time the pump status changed. In this way all peaks of the physical parameters are recorded in files of reasonable size. The present version of the model has been substantially refined and improved in terms of the coupling and convergence of the computational algorithm when compared with the preliminary results presented at the 14th International Drying Symposium.[14]

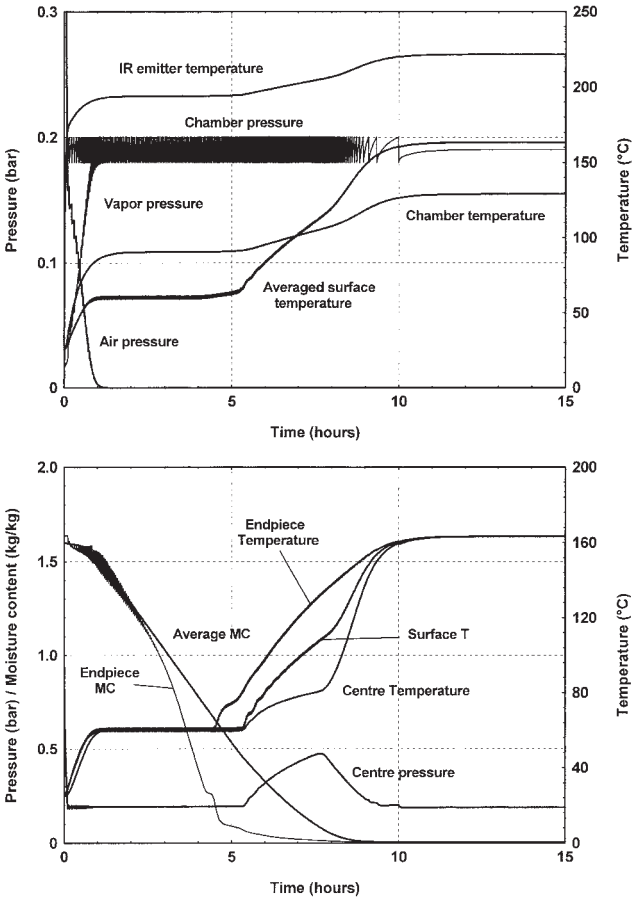

Figure 4. (a) Evolution of gas dynamics and (b) drying kinetics in the vacuum chamber for Case Study 1—Strong pump and well-insulated chamber.

Table 1. Physical Constants Used for the Simulations

Vacuum Chamber Conditions and Material Properties	Values Used for the Computations
Initial moisture content	150%
Initial temperature	25°C
Porosity	0.733
Density of solid matrix	400 kg m^{-3}
Transverse direction	
Intrinsic liquid permeability	2×10^{-14} m^2
Intrinsic gas permeability	4×10^{-15} m^2
Longitudinal direction	
Intrinsic liquid permeability	5×10^{-12} m^2
Intrinsic gas permeability	1×10^{-12} m^2
Wood cross section	1.3 × 22.5 × 15 cm
Chamber characteristics	
Minimum operating pressure	0.18 bar
Maximum operating pressure	0.20 bar
Volume of chamber	0.1 m^3
Dimensions of chamber (cylinder)	radius 0.21 m, height 0.72 m
Mass of IR emitters	0.5 kg
Mass of chamber wall	10 kg
Pump flow rate	2.0 m^3 h^{-1}
External temperature	25°C
External heat transfer coefficient	2.5 W m^{-2} $°C^{-1}$
Electrical power	320 W

Results and Discussion

The results computed by the coupled model are shown in Figure 4a for the evolution of the gas dynamics in the chamber and in Figure 4b for the overall drying kinetics. The important physical wood properties used for the simulations are summarized in Appendix B and the chamber values are summarized in Table 1. The permeability values are the same as those used in the macroscale model for the same configuration.[13] For all simulations, we exaggerated the gap between the minimum (0.18 bar) and maximum (0.2 bar) pressure levels to emphasize the coupling between the two scales.

At the very beginning of the process, the chamber pressure equals the atmospheric pressure and the gas mixture consists chiefly of air. The pump operates at first to decrease the total pressure and then, as drying starts, a flux of vapor coming from the board increases the chamber pressure. The vacuum pump has to be switched on regularly and, subsequently, the air part of the gas mixture reduces stepwise and the partial pressure of vapor increases. At around 1 h (Figure 4a), the chamber contains mostly only vapor. The electrical power supplied to the IR emitters heats the emitters at first and, as a result of radiative heat transfer, heats the chamber and the board. During the constant drying rate period (surface temperature close to the boiling point of water), a quasi-steady-state regime arises, during which the thermal fluxes are almost constant: one important part of this flux supplies the heat of vaporization and the remaining part compensates for thermal losses through the chamber walls. At the end of drying, because the need for vaporization diminishes, the chamber temperature increases and the final steady-state regime is such that the IR emitter fluxes compensate the thermal losses through the chamber. For this well-insulated chamber, the chamber walls always remain above the dew point and no condensation can be observed. Con-

sequently, all the vapor exiting the board has to be removed from the chamber by the vacuum pump. This is exactly what was used in our experiment to gather the drying kinetics.[13] In this case, a highly oscillatory behavior of the chamber pressure during the drying process is evident. This behavior arises from the coupling between the pump flux and the moisture flux leaving the board. The pump flux together with the chamber volume defines a time constant for the pressure evolution when the pump is on (maximum allowable pressure attained), resulting in pressure-decreasing periods. Obviously, the moisture flux leaving the board tends to increase this characteristic time. Once the minimum pressure is reached, the pump is switched off, leading to a pressure increase that is proportional to the ratio between the chamber volume and the drying flux. In the present case, because of the high drying rate and the strong pump, both time constants (increasing and decreasing periods) are small, thus explaining the high frequency of oscillations observed in Figure 4a.

As stated in previous work by the authors, Figure 4b highlights that this configuration of vacuum drying with radiative heating resembles a configuration of convective drying at high temperature. After the transient heating period, a plateau arises at the dew point temperature, which is also the boiling point for this configuration of pure vapor. This is the constant drying rate regime. As a consequence of the variable boundary conditions of the macroscale model, the oscillatory behavior of the chamber can also be observed on the board parameters. Note however that, because of the high frequency, the oscillation appears only as a thickening of the line (Figure 4b). By zooming in on the curves, one can discover that the amplitude peak to peak attains almost 2°C for the surface temperature. Because the longitudinal thermal conductivity of wood is twice that of the transverse direction, the amplitude is only about 1°C for the surface temperature at the end piece. Finally, as a result of the damping arising from internal heat transfer, the amplitude is reduced to 0.03°C for the center temperature. The amplitude is also noticeable for the moisture content at the end piece. This periodic variation has to be analyzed as a coupled and complex mechanism: the variation in chamber pressure has an influence on the internal pressure, which induces liquid migration along the longitudinal direction of the board and which is its most permeable direction. Consistent with a configuration of drying at high temperature, an internal overpressure appears inside the product at the end of the constant drying rate period, when the internal temperature rises above the boiling point of water while liquid water is still present in the core of the product. After 10 h of drying, the process is finished, the pump is switched off, and the oscillations cease (Figure 4a).

Experimental results obtained for a fir sapwood board of fir with similar conditions are presented in Figure 5.[13] Clearly the trends depicted by the model are consistent with these experimental results, with the drying time, constant drying rate

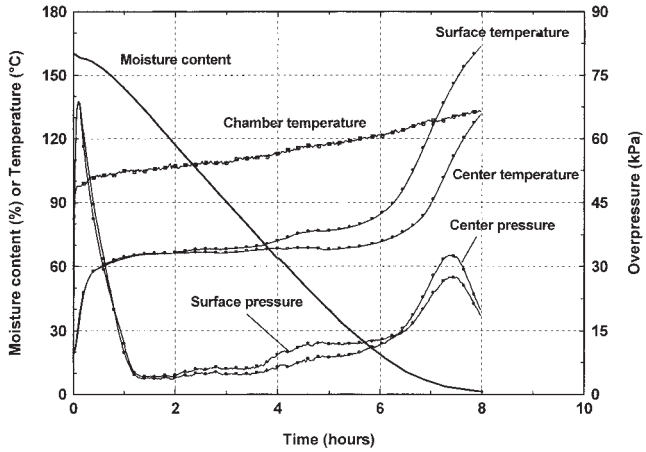

Figure 5. Radiative-vacuum drying of fir (*Abies alba*), sapwood.

$P_{chamber}$ = 200 mbar (Test 15; after Perré et al.[13]).

period, overpressure, board temperature, and chamber temperature evolution well captured by the model.

At this point, we have to keep in mind that the parameters used in the dual-scale model in the first case study (Figure 4) are those of a laboratory experimental device, which was well insulated, and the pump was strong enough to remove all the vapor from the chamber. Indeed, this device was designed to reconstitute the drying curve only by the vapor condensed at the outlet of the Teflon® vacuum pump. Three other case studies are now proposed to illustrate the potential of the dual-scale model to investigate, design, or improve other situations that are more representative of an industrial configuration.

Details and relevant parameters for these case studies are summarized in Table 2:

- Case study 2: well-insulated chamber and weak pump
- Case study 3: poorly insulated chamber and weak pump
- Case study 4: same as case study 1, but using a less permeable board

In Figure 6a, for the well-insulated chamber, it can be seen that the pump is not always able to maintain the pressure in the chamber within the desired range of 0.18–0.2 bar. The pump remains on while the drying rate is sufficiently large (up to 8 h here). This is why no air can exist in the chamber. The total pressure, which is also the partial vapor pressure, increases while the vapor density is sufficient for the pump flow rate to equilibrate the drying rate (the pump is a volumetric pump). Under the present conditions, the equilibrium is obtained for a pressure close to 0.5 bar. This pressure level produces a boiling temperature of 80°C, which is, accordingly, the board temperature

Table 2. Values Used in the Different Case Studies

Number of Case Study	Parameters Values
Case study 1	Same as Table 1
Case study 2 (weak pump)	Pump flow rate = 0.5 $m^3\ h^{-1}$
Case study 3 (weak pump + weak insulation)	Pump flow rate = 0.5 $m^3\ h^{-1}$ External heat transfer coefficient = 5 $W\ m^{-2}\ °C^{-1}$
Case study 4 (less permeable wood)	Transverse permeability values divided by 10

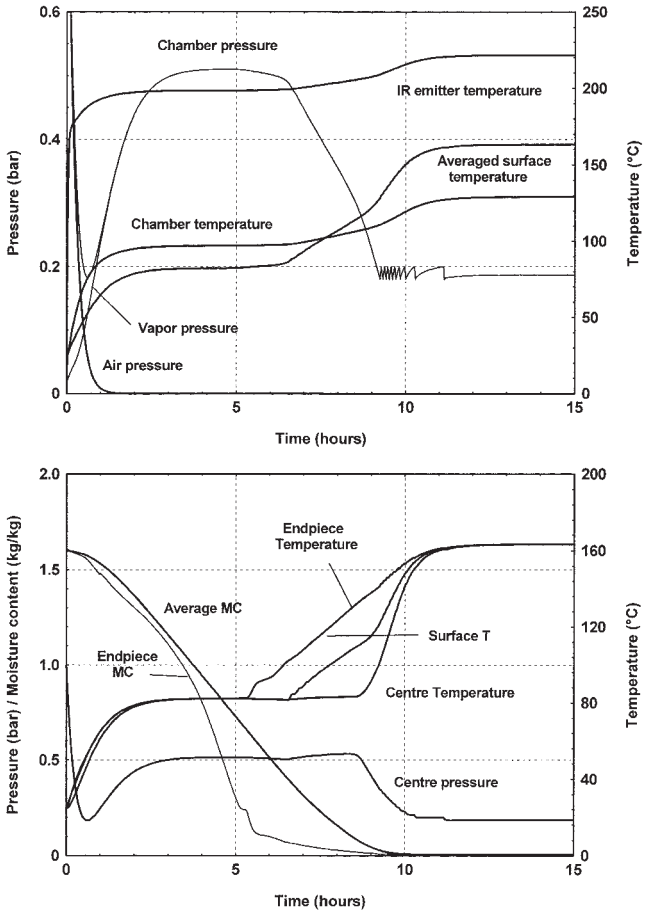

Figure 6. (a) Evolution of gas dynamics and (b) drying kinetics in the vacuum chamber for Case Study 2—weak pump and well insulated chamber.

during this first drying period. During the second drying period, the overpressure is almost negligible compared to that observed for case study 1. This can be explained by two opposing effects: the chamber pressure decreases because the drying rate decreases and the internal pressure increases as a result of increasing temperature. In fact, the internal overpressure, which is the difference between the center pressure and the chamber pressure, has almost the same magnitude as before.

Note, however, that keeping this weak pump in the case of a poorly insulated chamber for case study 3, a new mechanism can be observed (Figure 7). The first 2 h produce drying kinetics quite similar to that exhibited for case study 2. However, once the boiling temperature and thus the board temperature rise because of the increase in chamber pressure, these temperature values attain the chamber wall temperature. At this instant, condensation takes place within the chamber, producing a certain mass of liquid water at the bottom of the chamber (see the curve mass of water in Figure 7a), which subsequently limits the increase of pressure. During the first drying period, one part of the drying rate is removed from the chamber by the pump and the other part is just converted into liquid. This situation resembles that observed in industrial vacuum kilns where most of the water is extracted from the load by condensation on a cold plate controlled in temperature. Another consequence of the poor insulation is the low final levels of temperature (board and chamber) and the low drying kinetics. A period of 11 h is required for the averaged moisture content to attain 10% instead of the 7 h reported for case study 1.

Finally, for case study 4 we revisit the laboratory kiln (case study 1), but this time with a less permeable wood board having the transverse liquid and gaseous permeabilities divided by a factor of 10. As expected, the duration of the first drying period is reduced and, as a consequence, the internal pressure appears when the center moisture content is higher, with a much greater ability of liquid migration. Accordingly, the longitudinal liquid migration driven by the overpressure is able to resaturate the end piece (refer to Figure 8b at 4 h of drying). These mechanisms have been widely observed, simulated, and commented on in previous works (see, for example, Perré et al.[16] and Perré and Turner[20]). Also note—as additional effects of this reduced permeability—the more rapid increase in temperature, the higher level of overpressure during the second drying period, and the longer process duration.

Conclusions

The case studies reported herein highlight that the dual-scale model allows the intricate coupling that exists between the kiln (vacuum chamber) and the load to be accounted for throughout the

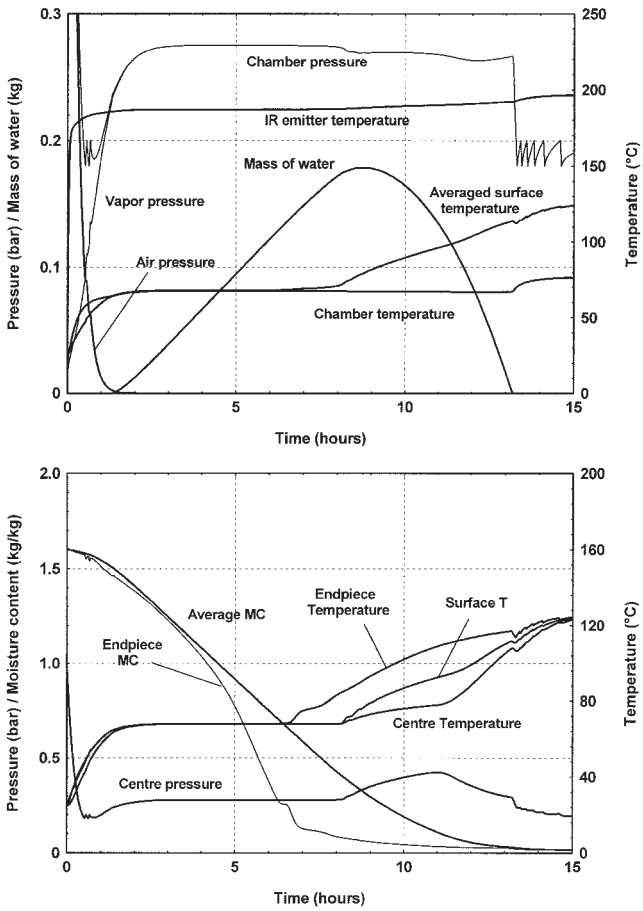

Figure 7. (a) Evolution of gas dynamics and (b) drying kinetics in the vacuum chamber for Case Study 3—Weak pump and poorly insulated chamber.

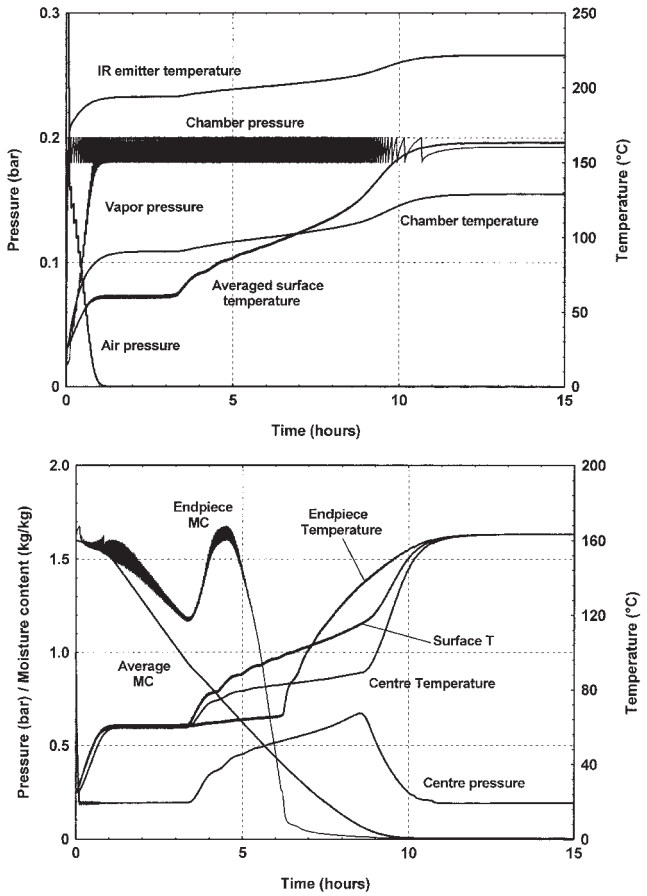

Figure 8. (a) Evolution of gas dynamics and (b) drying kinetics in the vacuum chamber for Case Study 4—Less permeable board.

drying process in a realistic and fairly accurate manner. The effectiveness and predictive ability of the underlying computational strategy required a combination of physical modeling, advanced experimental procedures, and state-of-the-art numerical analysis. Attention was paid to the influence of the pump flow rate and the chamber insulation on the vacuum drying process. The dual-scale model can predict some of the more subtle mechanisms observed in practice, such as the increase in the boiling point of water when the pump is too weak or the effect of vapor condensation when the insulation is insufficient. The model accounts automatically for the consequences of such modification to the transfer phenomena evolving inside the board.

It is hoped that the extensive information generated by this model during the simulations can be harnessed by drying engineers for the purposes of analyzing and optimizing existing drying operations, or for designing new drying procedures for a wide cross section of configurations and products. Future research will see the development of an on-line control model that uses this model as its core.

Literature Cited

1. Ressel BJ. State-of-the-art on vacuum drying of timber. Proceedings of the 4th International IUFRO Wood Drying Conference, Rotorua, New Zealand; 1994:255-262.
2. Joyet P, Meunier T. Drying green oak under vacuum with superheated steam without discoloration and drawback: Industrial results. Proceedings of the 5th International IUFRO Wood Drying Conference, Quebec, Canada; 1996:169-176.
3. Resch H, Gautsch E. High frequency current/vacuum lumber drying. Proceedings of the 7th International IUFRO Wood Drying Conference, Tsukuba, Japan; 2001:128-133.
4. Rozsa AN, Avramidis S. Radio frequency vacuum drying of eucalypt timbers. Proceedings of the 5th International IUFRO Conference, Quebec, Canada; 1996:135-139.
5. Tran N, Rozsa AN. Development of a novel radio frequency heating system for drying wood. Proceedings of the 6th International IUFRO Conference, Stellenbosch, South Africa; 1999:42-44.
6. Bird RB, Stewart WE, Lightfoot EN. *Transport Phenomena*. New York, NY: Wiley; 1960.
7. Masson EA, Malinauskas AP. *Gas-Transport in Porous Media: The Dusty-Gas Model* (Chemical Engineering Monographs 17). Amsterdam, The Netherlands: Elsevier; 1983.
8. Froment GF, Bischoff KB. *Chemical Reactor Analysis and Design* (Series in Chemical Engineering). New York, NY: Wiley; 1990.
9. Perré P, Joyet P, Aléon D. Vacuum drying: Physical requirements and practical solutions [Tutorial]. Proceedings of Vacuum Drying of Wood '95, High Tatras, Slovak Republic; 1995:7-34,
10. Joly P, More Chevalier F. *Théorie, pratique et économie du séchage des bois*. Dourdan, France: Éditions H. Vial; 1980.
11. Avramidis S. Radio-frequency vacuum drying of wood [Invited Conference]. Proceedings of the First COST Action E15 Wood Drying Workshop, Edinburgh, Scotland; 1999.
12. Bucki M. *Etude expérimentale et simulation numérique d'un procédé de séchage couplé vide et hautes fréquences: Application au bois de chêne*. PhD Thesis. Nancy, France: French Institute of Forestry, Agricultural and Environmental Engineering (ENGREF); 2004.
13. Perré P, Mosnier S, Turner IW. Vacuum drying of wood with radiative heating. Part I: Experimental procedure with local measurements of temperature and pressure. *AIChE J.* 2004;50:97-107.
14. Turner IW, Perré P. A new two-scale model describing drying kiln dynamics and coupled heat and mass transfer in a porous medium. Application to the combined vacuum drying and radiative heating of wood. Proceedings of the 14th International Drying Symposium, São Paolo, Brazil; 2004:436-443.
15. Cameron IT. Modern process modelling: Multiscale and goal-directed [Keynote address]. Proceedings of the 14th International Drying Symposium, São Paulo, Brazil; 2004:3-17.
16. Perré P, Moser M, Martin M. Advances in transport phenomena during convective drying with superheated steam or moist air. *Int J Heat Mass Transfer.* 1993;36:2725-2746.
17. Whitaker S. Simultaneous heat, mass, and momentum transfer in porous media: A theory of drying. *Adv Heat Transfer.* 1977;13:119-203.
18. Perré P, Degiovanni A. Simulation par volumes finis des transferts couplés en milieux poreux anisotropes: Séchage du bois à basse et à haute température, *Int J Heat Mass Transfer.* 1990;33:2463-2478.
19. Turner I, Perré P. A synopsis of the strategies and efficient resolution techniques used for modelling and numerically simulating the drying process. In: Turner IW, Mujumdar A, eds. *Numerical Methods and Mathematical Modelling of the Drying Process*. New York, NY: Marcel Dekker; 1996:1-82.
20. Perré P, Turner I. Using a set of macroscopic equations to simulate heat and mass transfer in porous media: Some possibilities illustrated by a wide range of configurations that emphasize the role of internal pressure. In: Turner IW, Mujumdar A, eds. *Numerical Methods and Mathematical Modelling of the Drying Process*. New York, NY: Marcel Dekker; 1996:83-156.
21. Perré P, Turner IW. Microwave drying of softwood in an oversized waveguide. *AIChE J.* 1997;43:2579-2595.
22. Perré P, Turner I. *TransPore*: A generic heat and mass transfer computational model for understanding and visualising the drying of porous media [Invited paper]. *Drying Technol J.* 1999;17:1273-1289.
23. Perré P, Turner I. A 3D version of TransPore: A comprehensive heat and mass transfer computational model for simulating the drying of porous media. *Int J Heat Mass Transfer.* 1999;42:4501-4521.
24. Turner IW, Perré P. Vacuum drying of wood with radiative heating. Part II: Transfer mechanisms analysed using the computational code. TransPore and a 2-D semi-analytical solution. *AIChE J.* 2004;50:108-118.
25. Jennings A, McKeown JJ. *Matrix Computation*. 2nd Edition. New York, NY: Wiley; 1992.

Appendix A: Summary of the Porous Medium Model (*TransPore*)

The macroscopic equations that govern the drying process are summarized as follows:

Water Conservation

$$\frac{\partial}{\partial t}\left(\varepsilon_\ell \rho_\ell + \varepsilon_g \rho_v + \bar{\rho}_b\right) + \nabla\cdot\left(\rho_\ell \bar{\mathbf{v}}_\ell + \rho_v \bar{\mathbf{v}}_g + \overline{\rho_b \mathbf{v}_b}\right) = \nabla\cdot\left(\rho_g \bar{\bar{\mathbf{D}}}_{eff} \nabla \omega_v\right) \quad \text{(A1)}$$

Energy Conservation

$$\frac{\partial}{\partial t}\left[\varepsilon_\ell \rho_\ell h_\ell + \varepsilon_g(\rho_v h_v + \rho_a h_a) + \bar{\rho}_b \bar{h}_b + \rho_o h_s - \varepsilon_g P_g\right] + \nabla\cdot\left[\rho_\ell h_\ell \bar{\mathbf{v}}_\ell + (\rho_v h_v + \rho_a h_a)\bar{\mathbf{v}}_g + h_b \overline{\rho_b \mathbf{v}_b}\right] = \nabla\cdot\left[\rho_g \bar{\bar{\mathbf{D}}}_{eff}(h_v \nabla \omega_v + h_a \nabla \omega_a) + \bar{\bar{\mathbf{K}}}_{eff} \nabla T\right] \quad \text{(A2)}$$

Air Conservation

$$\frac{\partial}{\partial t}\left(\varepsilon_g \rho_a\right) + \nabla\cdot\left(\rho_a \bar{\mathbf{v}}_g\right) = \nabla\cdot\left(\rho_g \bar{\bar{\mathbf{D}}}_{eff} \nabla \omega_a\right) \quad \text{(A3)}$$

Gaseous- and Liquid-Phase Velocities

$$\bar{\mathbf{v}}_i = -\frac{\bar{\bar{\mathbf{K}}}_i \bar{\bar{\mathbf{k}}}_i}{\mu_i} \nabla \varphi_i \qquad \nabla \varphi_i = \nabla P_i - \rho_i g \nabla \chi \qquad \text{where } i = \ell, g \quad \text{(A4)}$$

where φ is the phase potentials and χ is the depth scalar. All other symbols have their usual meaning. The liquid and gaseous pressures are related through the capillary pressure, which depends only on the moisture content:

$$P_\ell = P_g - P_c(X) \quad \text{(A5)}$$

Boundary and Initial Conditions

$$\mathbf{J_w} \times \hat{\mathbf{n}} = k_m c M_v \ln\left[\frac{1 - x_v^{(ch)}}{1 - x_v}\right]$$

$$\mathbf{J_e} \times \hat{\mathbf{n}} = h\left[T - T_v^{(ch)}\right] \quad \text{(A6)}$$

where $\mathbf{J_w}$ and $\mathbf{J_e}$ represent the fluxes of total moisture and total enthalpy at the boundary of the domain, respectively.

Initially the porous medium has some prescribed moisture content with the pressure and temperature being constant throughout the board at the atmospheric value and initial temperature, respectively.

Appendix B: Values Used in the Porous Medium Model (*TransPore*)

Because wood is highly hygroscopic, bound water has to be separated from free water:

$$X = X_b + X_{fw}$$

where $X_b = \min(X_{fsp}, X)$ and $X_{fsp} = 0.325 - 0.001T$ (at full saturation, $X_{sat} = X_{fsp} + X_{fw\,max}$).

The sorption isotherm is calculated according to the following expression:

$$\frac{P_v}{P_{vs}} = 1 - \exp[-X^* \times (0.764269 + 3.67872 \times X^*)] \qquad \text{with } X^* = \frac{X}{X_{fsp}}$$

The saturation variable involved in the relative permeability functions is calculated according to the free water content only:

$$S_{fw} = \frac{X_{fw}}{X_{fw\,\max}}$$

The physical data used for wood in this article are listed in Tables 1B and 2B.

Table 1B. Scalar Values

Material Properties	Values Used for the Computations
Heat capacity	$\overline{\rho C_p} = \rho_0(1113 + 4.85T + 4185X)$ (J kg^{-1} K^{-1})
Sorption isotherm	$\frac{P_v}{P_{vs}} = 1 - \exp(-0.76427A - 3.6787A^2)$ with $A = X_b/X_{fsp}$
Capillary pressure	$P_c = 1.24 \times 10^5 \sigma(S_{fw} + 1 \times 10^{-4})^{-0.61}$

Table 2B. Tensorial Values

Material Property	Transverse	Longitudinal
Gaseous diffusion	$D_{eff}^T = 4.10^{-3} \times k_{rg} D_v$	$D_{eff}^L = 4.10^{-2} \times k_{r\ell} D_v$
Bound water diffusion	$D_b^T = \left[-9.9 + 9.8X - \frac{4300}{T_k}\right]$	$D_b^L = 2.5 D_b^T$
Thermal conductivity (W m^{-1} K^{-1})	$\lambda_{eff}^T = 0.14 + 0.3X$	$\lambda_{eff}^L = 2\lambda_{eff}^T$
Liquid permeability (m^2)	2×10^{-14}	5×10^{-12}
Gaseous permeability	4×10^{-15}	1×10^{-12}
Liquid relative permeability	$k_{r\ell}^T = (S_{wf})^3$	$k_{r\ell}^L = (S_{wf})^8$
Gaseous relative permeability	$k_{rg}^T = 1 + (2S_{wf} - 3)(S_{wf})^2$	$k_{rg}^L = 1 + (4S_{wf} - 5)(S_{wf})^4$

Manuscript received Feb. 7, 2005, revision received Feb. 17, 2006, and final revision received Jun. 2, 2006.